West Point Research Papers

2-1-2022

Detailed Velocity and Heat Transfer Measurements in an Advanced Gas Turbine Vane Insert Using Magnetic Resonance Velocimetry and Infrared Thermometry

Michael Benson
United States Military Academy, michael.benson@westpoint.edu

David Bindon CDT'19
United States Military Academy, david.bindon@outlook.com

Mattias Cooper CDT'19
United States Military Academy, mattias.a.cooper.mil@mail.mil

F. Todd Davidson
United States Military Academy, frederick.davidson@westpoint.edu

Benjamin Duhaime CDT'19
United States Military Academy, benjamin.j.duhaime.mil@mail.mil

Follow this and additional works at: https://digitalcommons.usmalibrary.org/usma_research_papers

See next page for additional authors

Part of the Aerodynamics and Fluid Mechanics Commons, and the Heat Transfer, Combustion Commons

Recommended Citation

Authors

Michael Benson, David Bindon CDT'19, Mattias Cooper CDT'19, F. Todd Davidson, Benjamin Duhaime CDT'19, David Helmer, Robert Woodings CDT'19, Bret P. Van Poppel, Christopher J. Elkins, and John P. Clark

Michael J. Benson[1]
Department of Civil and Mechanical Engineering,
United States Military Academy,
West Point, NY 10996
e-mail: michael.benson@westpoint.edu

David Bindon
Department of Civil and Mechanical Engineering,
United States Military Academy,
West Point, NY 10996
e-mail: david.bindon@outlook.com

Mattias Cooper
Department of Civil and Mechanical Engineering,
United States Military Academy,
West Point, NY 10996
e-mail: mattias.a.cooper.mil@mail.mil

F. Todd Davidson
Department of Civil and Mechanical Engineering,
United States Military Academy,
West Point, NY 10996
e-mail: frederick.davidson@westpoint.edu

Benjamin Duhaime
Department of Civil and Mechanical Engineering,
United States Military Academy,
West Point, NY 10996
e-mail: benjamin.j.duhaime.mil@mail.mil

David Helmer
Department of Civil and Mechanical Engineering,
United States Military Academy,
West Point, NY 10996
e-mail: david.helmer@westpoint.edu

Robert Woodings
Department of Civil and Mechanical Engineering,
United States Military Academy,
West Point, NY 10996
e-mail: robert.t.woodings2.mil@mail.mil

Bret P. Van Poppel
Department of Civil and Mechanical Engineering,
United States Military Academy,
West Point, NY 10996
e-mail: bret.vanpoppel@westpoint.edu

Christopher J. Elkins
Department of Mechanical Engineering,
Stanford University,
Stanford, CA 94305
e-mail: celkins@stanford.edu

John P. Clark
Aerospace Systems Directorate
Air Force Research Laboratory,
Wright Patterson AFB, OH 45433
e-mail: john.clark.38@us.af.mil

Detailed Velocity and Heat Transfer Measurements in an Advanced Gas Turbine Vane Insert Using Magnetic Resonance Velocimetry and Infrared Thermometry

This work reports the results of paired experiments for a complex internal cooling flow within a gas turbine vane using magnetic resonance velocimetry (MRV) and steady-state infrared (IR) thermometry. A scaled model of the leading edge insert for a gas turbine vane with multi-pass impingement was designed, built using stereolithography fabrication methods, and tested using MRV techniques to collect a three-dimensional, three-component velocity field data set for a fully turbulent test case. Stagnation and recirculation zones were identified and assessed in terms of impact on potential cooling performance. A paired experiment employed an IR camera to measure the temperature profile data of a thin, heated stainless steel impingement surface modeling the inside turbine blade wall cooled by the impingement from the vane cooling insert, providing complementary data sets. The temperature data allow for the calculation of wall heat transfer (HT) characteristics, including the Nusselt number distribution for cooling performance analysis to inform design and validate computational models. Quantitative and qualitative comparisons of the paired results show that the flow velocity and cooling performance are highly coupled. Module-to-module variation in the surface Nusselt number distributions is evident, attributable to the complex interaction between transverse and impinging flows within the apparatus. Finally, a comparison with internal HT correlations is conducted using the data from Florschuetz et al. [1981, "Streamwiseflow and Heat Transfer Distributions for Jet Array Impingement With Crossflow," ASME 1981 International Gas Turbine Conference and Products Show, American Society of Mechanical Engineers. doi:10.1115/1.3244463]. Measurement uncertainty was assessed and estimated to be approximately ±7% for velocity and ranging from ±3% to ±10% for Nusselt number. [DOI: 10.1115/1.4052310]

Keywords: impingement cooling, IR thermography, MRV, turbine vane cooling, convective heat transfer

---

1 Introduction

Gas turbine engines provide a useful source of power for military and civilian aircraft, electrical generation, and many other applications. The engine components, especially the turbine vanes, are subject to high temperatures and pressures in order to increase the
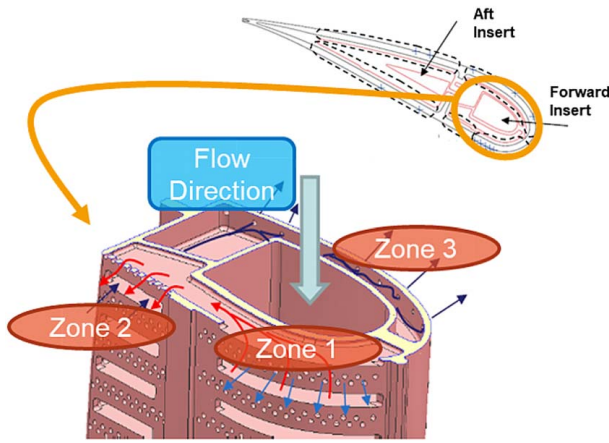
Fig. 1 Vane insert detail showing flow paths

thermal and overall system efficiency [1,2]. Increasing internal engine temperature has a positive effect on thermal efficiency, but the higher combustion temperatures can often exceed the melting temperature of the internal materials [1,2]. The utilization of air bypassing the combustion stage is a commonly accepted practice for engine component cooling with the most effective use of the cooling air being a widely researched area [3–14]. Impinging jets, used in a variety of engineering applications for highly efficient heat removal, have been extensively studied in general, as in Refs. [15–19] among many others, and in turbomachinery applications to cool the internal surface of blades and vanes [20–22]. Complex internal geometries are often implemented in engines using vane inserts to deliver impingement cooling.

Over the past decade, a stage-and-one-half transonic turbine was developed at the Air Force Research Laboratory (AFRL) [23] to improve the understanding of unsteady flows and heat transfer (HT) in a full-scale, rotating turbine stage consistent with a Generation 6 engine study cycle. This turbine was used successfully to benchmark conjugate HT analysis against experimental data from a fully cooled three-dimensional nozzle guide vane [24] as well as to demonstrate the potential to use aerodynamic design techniques to reduce unsteady shock interactions that occur when the vane downstream of the stage is consistent with the inlet-guide-vane of a counter-rotating low pressure turbine [25]. Additionally, an attempt was made to employ design optimization techniques to improve the cooling distribution over the pressure side of the nozzle guide vane [26]. In the course of validating the optimized cooling design, it became clear that the sensors within the experimental turbine suffered from a high attrition rate. The loss of sensors is detrimental to making judgements about the efficacy of design variations. This is because direct comparison of the heat

flux at the same airfoil surface location between any two different cooling designs requires the survival of as many as four sensors over the lifetime of the experiment [27]. The next phase of the turbine experimental program involves the evaluation of a pair of internal cooling designs installed in the inlet guide vane: a standard impingement array and a multi-impingement array. It is expected that the inclusion of internal cooling schemes in conjunction with external film cooling distributions will further complicate any comparison of the designs made with existing measurement capabilities available in the full-scale turbine experiment. Accordingly, the effort presented in this paper was executed to supplement and complement the data that will be available at the end of the experiments conducted at full-scale in the transonic, rotating turbine stage.

This work seeks to characterize the thermal performance of an advanced multi-impingement array vane insert design of the first type described in Ref. [28] which shares some similar characteristics to the device described in Ref. [29]. The present system is a large-scale representation of the internal cooling features developed by Florida Turbine Technologies (FTT) for insertion into the leading edge of a vane in a rotating turbine experiment at the AFRL. The complete vane has both a forward and an aft insert as shown in Fig. 1. These two inserts are designed to cool the inside surface of turbine vanes through impingement and film cooling methods. This work studies the performance of impingement cooling within the forward insert only. The forward insert of the vane cooling design consists of 23 modules from top to bottom, as shown in Fig. 2, and three separate impingement cooling zones in each module. After entering the insert via the main feed cavity at the top, the flow is diverted to the first impingement zone running along the pressure side of the vane and including the leading edge. The flow then recirculates, impinges on the pressure side in the second impingement zone, before recirculating again and impinging a final time on the suction side. The fluid is eventually extracted from the insert either through the trailing edge of the vane or through film cooling holes along the vane surface.

This paper reports the results of paired experiments of a complex internal cooling flow within a gas turbine vane using magnetic resonance velocimetry (MRV) and steady-state infrared (IR) thermometry. A scaled model of the vane cooling insert's leading edge was designed, built using stereolithography (SLA) fabrication methods, and tested using MRV techniques to collect three-dimensional, three-component velocity field data sets for a fully turbulent test case. The MRV tests were used to develop velocity fields within the inserts. A paired experiment employed an IR camera to measure the temperature profile data of a thin sheet, stainless steel impingement surface modeling the vane cooling insert, providing complementary data sets. The temperature data allow for the calculation of surface HT characteristics, including the Nusselt number distribution for cooling performance analysis. This work advances the state-of-the-art by coupling detailed velocimetry and HT data to fully characterize the thermal performance of turbomachinery
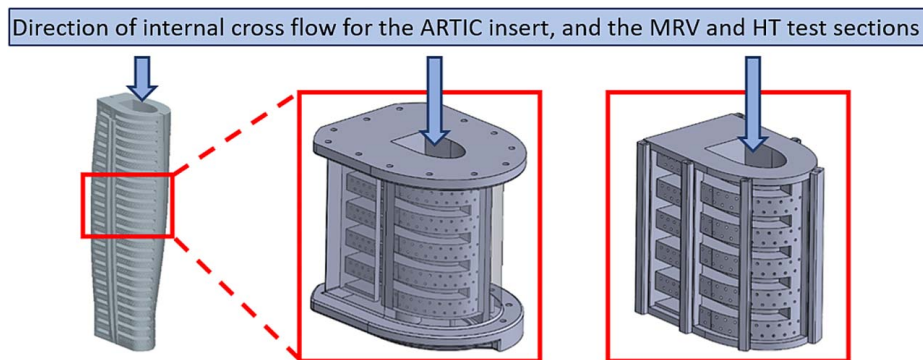

Fig. 2 Comparison of vane cooling insert (left), MRV test section (center), and HT test section (right). Note that MRV test section (center) and HT test section (right) images are rendered with transparent outer walls to highlight device similarity.

components with complex geometries and internal flow paths. In doing so, this work can be used as a baseline data set to validate computational models and directly inform designs of advanced gas turbine engine components.

2 Background

One obstacle in designing the internal geometries of gas turbine components is the ability to accurately measure flow and HT characteristics. The process for measuring three-dimensional velocity data in complex internal geometries presents a unique challenge due to the need for optical access, integration of probes into the flow path, or simplification of component geometry. Some of the common practices for measuring velocity are the use of two-dimensional particle image velocimetry, laser Doppler anemometry, and advanced laser techniques [30,31]. MRV, as used in this work, provides the unique capability of measuring three-component, three-dimensional velocity field data sets of laminar or turbulent flows in complex geometries without flow-disturbing probes and requiring no optical access [32]. This method leverages the nuclear resonance in hydrogen protons [33,34] in order to determine the velocity of small volumes of fluid or voxels [32,37]. The MRV experimental method provides the ability to obtain velocity fields that would be difficult to obtain using other methods and uniquely offers benefits of low measurement uncertainty, short testing times, and well-defined boundary conditions.

Measurement techniques to determine local HT characteristics have focused on the transient cooling response, such as liquid crystal thermography [36,37]. Steady-state IR testing employs Joule heating on a thin sheet formed to the desired geometry and brought to a prescribed boundary condition [38]. The use of a steady-state IR technique allows for measurement of temperature data in a single image as opposed to a series of images for a transient technique and allows for rapid testing [38]. Overlaying multiple images during steady-state testing further reduces error. This technique enables mapping the local HT coefficients across the surface of the imaged geometry to inform areas that require further cooling. A similar method has been used by other researchers to determine relevant HT coefficients for turbine components, including the effect of HT augmentation due to film cooling [39,40]. Others have used the Joule heating method to study the performance of impingement cooling [41–43], with the Imbriale work [42] reporting peak Nusselt numbers between jets for some cases, attributable to vortical structure formations between jets that enhance convective HT between the holes' centerlines.

Computational simulations provide a cost-effective tool to estimate the performance of a system, but this approach requires substantive validation and is very sensitive to inlet and boundary conditions and other factors [4,44–47]. Increasing computational power has aided the growth and development of numerical techniques, which when validated against robust data sets can provide excellent insight into fundamental flow features that are difficult to experimentally measure. The use of MRV to accurately and efficiently measure velocity through a test section and steady-state HT to characterize the system's thermal response offers a robust validation data set. The volume of data obtained through these experiments is large, providing orders of magnitude more data points than most traditional experiments. Benson et al. [48] showed that one MRV test provided over 4.2 million locations, each with three-component velocity data, which is on the order of a reasonable computational mesh for the domain studied. Combining MRV and IR tests enables computational model validation with high resolution data sets.

3 Experimental Setup and Analytical Methods

The test geometry was inspired by the vane cooling insert system [17,29]. For this test, only the forward insert was modeled, which consists of three separate cooling zones, as depicted in Fig. 1. The flow direction indicated in Fig. 1 represents coolant flowing

Table 1 Comparison of vane cooling insert and test sections for completing velocimetry and HT tests

Parameter	Vane cooling insert	MRV test section	HT test section
Scale	1:1	1:6.67	1:4.66
Impingement hole diameter	0.381 mm	2.54 mm	1.77 mm
Working fluid	Air	Water	Air
Inlet Reynolds number	10,000	10,000	10,000

in the radial direction within the vane (e.g., from tip to root through the insert). This flow direction will be referred to as the streamwise direction for internal crossflow. Experiments were conducted in two parts: (1) time-averaged, three-dimensional, three-component velocity measurements using MRV and (2) steady-state HT measurements using IR thermography. The MRV experiments were completed in the Richard M. Lucas Center for Radiology at Stanford University. The HT tests were completed at the U.S. Military Academy at West Point. Experimental rigs for both tests were manufactured to meet the specific dimensions of the testing facilities, while maintaining similitude with the vane cooling insert developed by FTT and AFRL. The HT rig was manufactured using SLA with a Viper Si2 printer using Accura 60 resin; both printer and resin are made by 3D Systems, Incorporated. The use of SLA manufacturing methods enables complex wall geometries using materials that can be thermally and electrically insulating. The MRV and HT experimental rigs were designed to approximate the behavior of fluid within the mid-span of the vane cooling insert. A comparison of the respective experimental test sections is provided in Fig. 2. Table 1 summarizes key parameters for the actual vane cooling insert, the MRV test section, and the HT test section.

3.1 Magnetic Resonance Velocimetry. The MRV results were obtained using a 3.0 Tesla GE Signa Pioneer Magnetic Resonance Imaging (MRI) scanner. The imaging matrix was $222 \times 300 \times 166$ volumetric elements (voxels) with an isotropic resolution of 0.8 mm. A single scan time lasted 473 s. A full data set was defined as 12 scans during which the flow was on, and seven scans with the flow off. The order in which these scans were taken was one with no flow followed by two with flow on (off-on-on-off, etc.). This sequence accounts for any change in the background noise produced by the MRI scanner over time.

The test section shown in the center image of Figs. 2 and 3(*a*) was built specifically for MRV testing. This rig consists of five modules as opposed to 23 in the vane cooling insert. The scale selected for MRV testing was 1:6.67. An inlet section, shown in Fig. 3(*b*), includes two gridded inserts to distribute the flow as the internal shape changes from circular to non-circular. A tip bleed was introduced at the end of the main feed cavity, below the outlet in Fig. 3(*a*), allowing some of the bulk flow to bleed out of the system. This feature's purpose was twofold: first, it prevented stagnation at the end of the main feed cavity to better model modules at the root of the vane cooling forward insert; and second, it provided independent control of impingement jet velocities and the Reynolds number within the main feed cavity. Additional details of the MRV test section are available in Ref. [17].

Velocity fields within the test section were collected for a fully turbulent Reynolds number based on the hydraulic diameter of the inlet section, Re = 10,000, at an inlet flowrate of 37.2 L/min. The tip bleed accounted for 45% of the flow exiting the system. The overall schematic for MRV testing is displayed in Fig. 4(*a*). As shown, the temperature of the fluid was maintained using a cold fluid reservoir, and flowrates were controlled by ball valves. Flowrate was measured directly at the inlet and tip bleed using an ultrasonic flowmeter with measurement uncertainty of ± 0.075 L/min, or $\pm 1\%$. Figure 4(*b*) shows the experimental rig
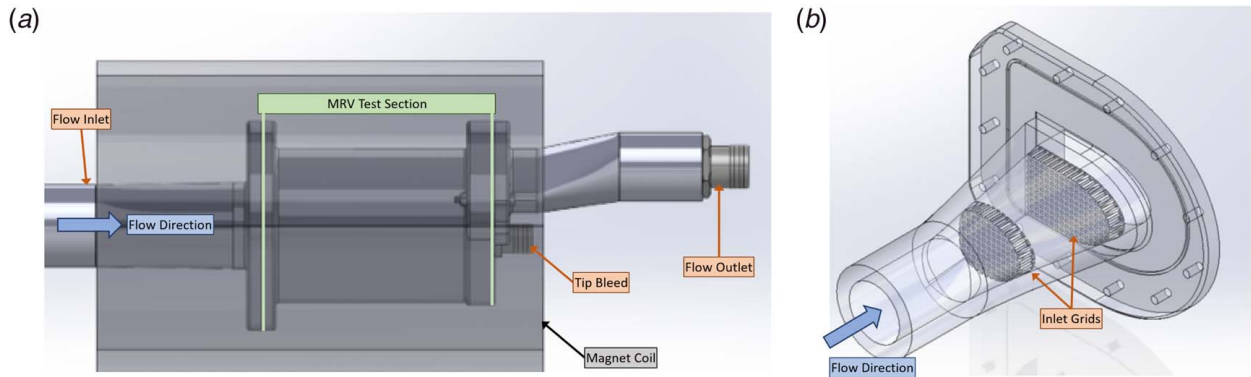
Fig. 3 Experimental test section employed in MRV, illustrating the flow outlet and tip bleed (left) and inlet with successive gridded inserts for flow conditioning (right). (*a*) primary test section, highlighting outlet and tip bleed and (*b*) test section inlet.
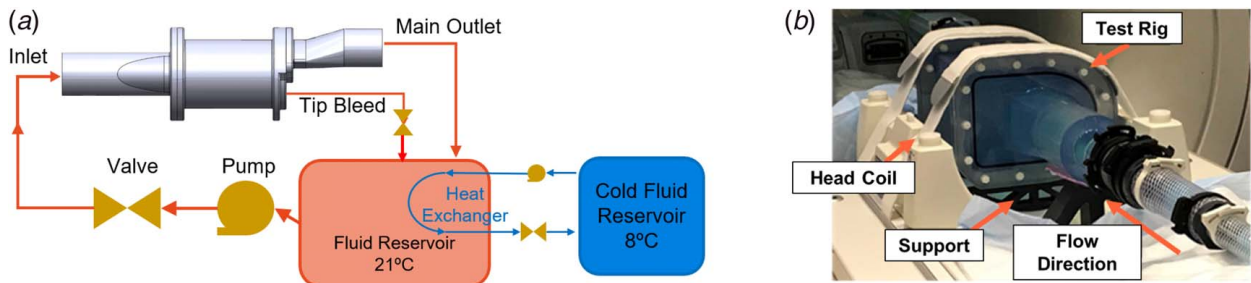

Fig. 4 Full MRV setup: flow loop schematic (left) and MRV test section with coil and in magnet (right). (*a*) MRV setup schematic and (*b*) MRV test section.

that houses the MRV test section, including a portion of the MRI head coil at the entrance to the magnet.

3.2 Heat Transfer Test. The test section for the HT rig varied in several ways from the MRV rig, but overall geometric similarity was maintained. The HT test used a similar setup to that in Ref. [38]. The HT test section is illustrated in Fig. 5(*a*). The test section was reduced to 70% of the scale of the MRV test section (i.e., a scale of 1:4.67), a design decision to permit greater temperature across the impingement surface and, subsequently, lower relative uncertainty for the HT test measurement. The HT test section had a hydraulic diameter of 0.0465 m, and it eliminated the SLA shell that was used in the MRV tests. Stainless steel shim with a

thickness of 0.13 mm was used to cover the impingement zones for the HT experiments. The stainless steel was painted with a matte black to increase the emissivity. Copper bus bars were used at the top and bottom of each shim to distribute electrical power evenly across the shims. The SLA test section, stainless steel shim, and copper bus bar were attached mechanically. The assembly was sealed with both epoxy and silicone adhesive to eliminate leaks. A schematic of the final assembly is shown in Fig. 5(*c*). Prior to the experiment, fiducial marks were made along the top and bottom of each shim, spaced 3.2 mm apart.

Impingement zones one and three were subdivided into two smaller zones, depicted in Fig. 5(*b*). These subdivisions allowed for smaller regions to be powered and imaged individually. The divisions do not extend into the impingement zones themselves,
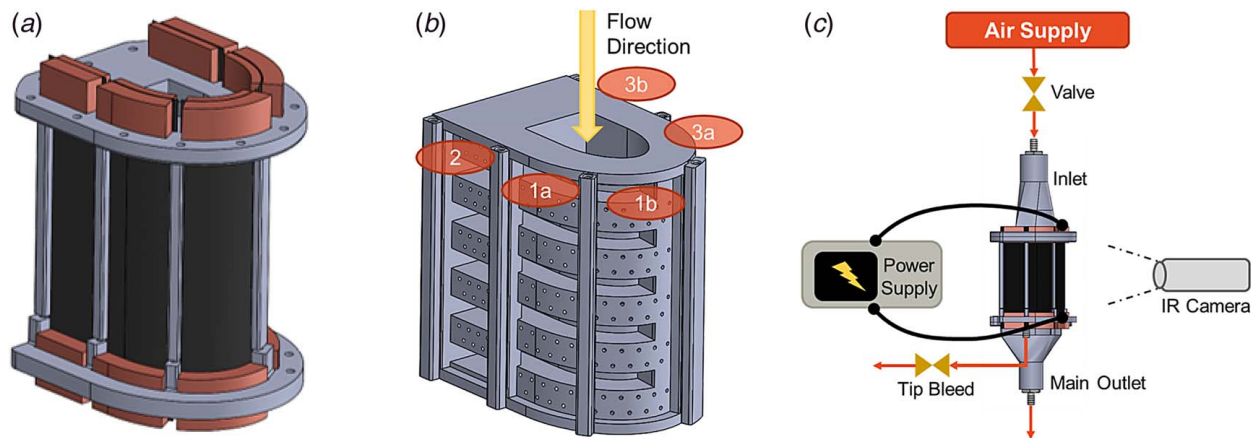

Fig. 5 HT test section highlighting installed stainless steel, matte black shims and copper bus bars (left), geometry with five sections (center), and air inlets and exits and IR camera position (right). (*a*) HT test section, (*b*) HT test section geometry, and (*c*) HT full setup.

021009-4 / Vol. 144, FEBRUARY 2022   **Transactions of the ASME**
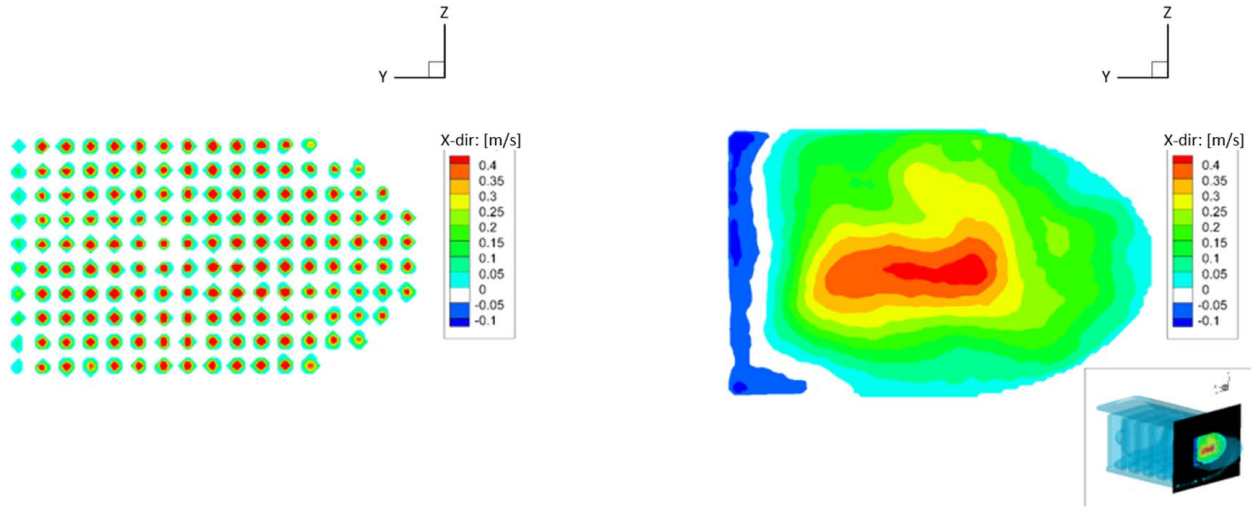
Fig. 6 Inlet velocity profiles (m/s). Left image shows profile through flow conditioning grates. Flow is into page.

so air is free to flow laterally across all three zones as it does in both the vane cooling geometry and the MRV test section.

Prior to collecting data on the HT rig, the system was brought to steady state. Compressed air was supplied to the test rig, and the flowrate was monitored with two Omega FMA 1600-series flowmeters (uncertainty $<\pm 1\%$). Using a FLIR model A655sc long wave form IR camera (15 deg field of view), sequential images were taken of the rig surface to confirm that the assembly had reached steady state. Once at steady state, the resultant surface temperature was used to estimate the temperature of the supplied air. This method of temperature measurement was preferred to a separate thermocouple measurement to reduce bias error associated with the camera when computing the temperature difference used in the calculation of the convective cooling rate.

A Sorensen XFR 12-220 power source was used to produce a constant heat flux boundary condition across the shim using electric resistance heating. The power source provided a measurement of the current flowing through the assembly, and a voltmeter was used to determine the voltage drop at the top and bottom of the shim to ensure uniform current distribution. The power into the shim was estimated as the product of the current and voltage drop across the shim, expressed as,

$$\dot{Q}_{\text{Joule}} = I \cdot V \qquad (1)$$

where I is the electric current (A) and V is the steady-state voltage (V). The heated surface was imaged with the IR camera. Air flow entering the SLA model provided convective cooling on the interior surface of the heated shim. The high-temperature steady-state condition was established within a few minutes, with the time to reach steady state depending on power supplied and air flowrate. Several IR images were taken during a run, providing the temperature of the surface and surroundings. To image different zones of the test section, the camera was relocated to minimize the viewing angle.

An energy balance was used to solve for the HT coefficient of the cooling air, with Eq. (2) written on a rate basis,

$$\dot{Q}_{\text{conv}} = \dot{Q}_{\text{Joule}} - \dot{Q}_{\text{cond}} - \dot{Q}_{\text{natural}} - \dot{Q}_{\text{rad}} \qquad (2)$$

where $\dot{Q}$ is the HT rate. The total power input to the test section is given in Eq. (1). The power applied to each pixel can be computed by a factor equivalent to the ratio of pixel-to-plate surface areas. The thermal energy lost due to conduction can be found using a basic conduction nodal analysis assuming that each pixel is small enough to maintain a uniform temperature, as

$$\dot{Q}_{\text{cond}} = k(T_{m,n-1} + T_{m,n+1} + T_{m-1,n} + T_{m+1,n} - 4T_{m,n}) \qquad (3)$$

with m and n representing the indices in a two-dimensional x–y plane stenciled onto a uniform grid ($\Delta x = \Delta y$) with a unit depth ($\Delta z = 1$), $T_{m,n}$ the temperature at the node of interest, and common assumptions of constant thermal conductivity and steady-state behavior [49]. Natural convection was assumed negligible using estimated values for thermo-physical properties and an order of magnitude comparison of Grashof and Reynolds numbers:

$$\frac{\text{Gr}}{\text{Re}^2} \ll 1$$

Radiation was assumed negligible based on the relatively small temperature difference between the experimental rig and the ambient room temperature.

4 Results

4.1 Velocity Measurements. Figure 6 shows a representative inlet profile using the MRV method at an inlet Reynolds number of 10,000 based on hydraulic diameter at the inlet shown in Fig. 3(b) just downstream of the inlet grids. The profile was taken after the flow passed through flow straighteners, but before it entered the feed cavity within the vane cooling insert geometry. This result can provide an inlet boundary condition for CFD. Note in Fig. 6 that the direction of the flow is along the positive x-axis, with the y and z coordinates representing the radial direction. In the bottom right corner is an inset showing the position of the figure within the overall geometry of the test section.

Figure 7(a) illustrates the streamwise flow velocity. This view shows the impingement holes within zone 3b at the top of the figure and holes across the center of zone 2 at the bottom of the figure. The high velocity of the impingement jets can also be seen as small, bright columns at the top of Fig. 7(a). Figure 7(b) shows jet-to-jet interaction with extraction across both multiple modules and rows. There are slight differences between the three jet pairs based on their locations within each module. This observation suggests that there may be corresponding differences in HT performance across these locations as well and is a clear indicator that three-dimensional effects are important for the jet flows. For example, it is evident that the second module depicted in Fig. 7(b) has one jet highly impacted by these effects in zone 2, which is not apparent in the other jet pairs in neighboring modules. The row location, which also differs, is another contributing feature, and the corresponding effects on HT performance will be shown in Secs. 4.2 and 4.3.

Figures 8(a) and 8(b) show the return channel from zone 1 to zone 2 and zone 2 to zone 3, respectively, at approximately the
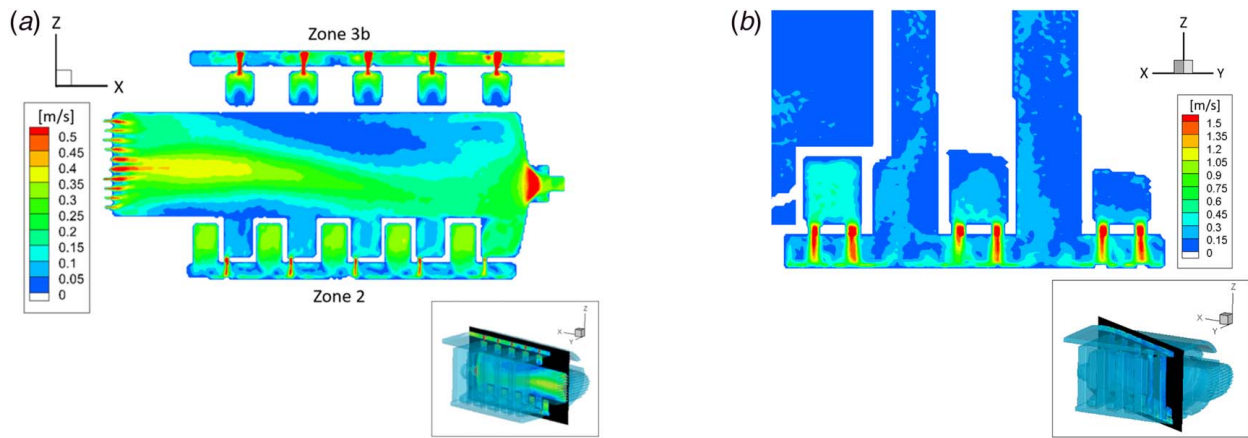
Fig. 7 Velocity magnitude in main feed cavity for two different views: (*a*) spanwise centerplane showing velocity magnitude and (*b*) transverse cut.
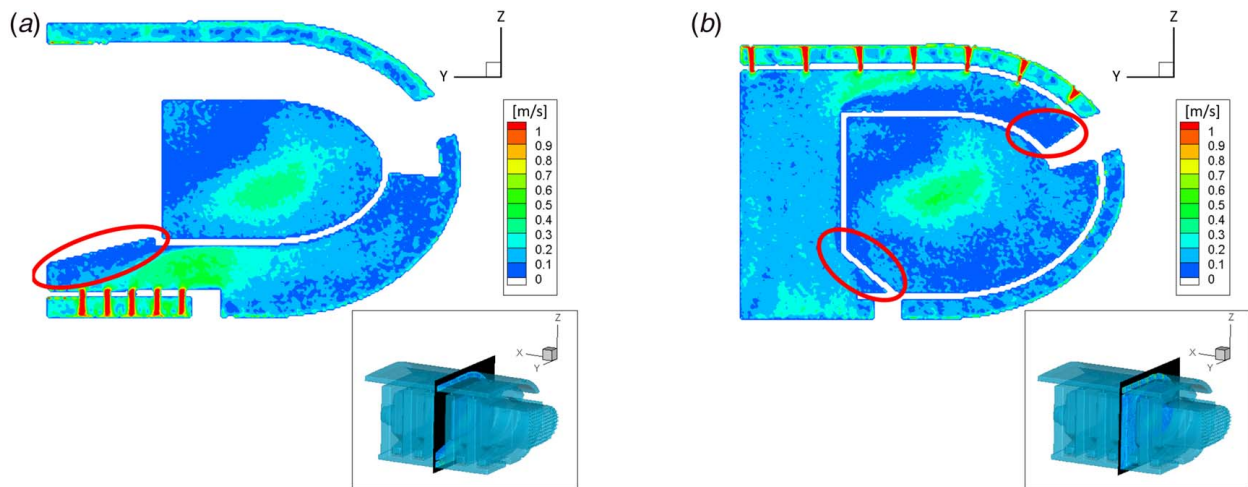

Fig. 8 Velocity magnitude along radial planes: return channel between zone 1 and zone 2 (left) and between zone 2 and zone 3 (right). Ovals highlight regions of low-speed flow and recirculation. (*a*) Return channel between zone 1 and zone 2. (*b*) Return channel between zone 2 and zone 3.

mid-span of the test section. Figure 1 can help orient the reader to the direction of flow within Figs. 8(*a*) and 8(*b*). The regions circled in these figures highlight locations within the internal vane cooling insert geometry that can be altered to improve the flow path. These areas are characterized by low-speed flow and recirculation. Improving the flow path has the potential to increase the efficiency with which heat can be removed from the vane surface. In each of these cases, the flowrate was at or below 0.1 m/s in the majority of each identified zone.

4.2 Heat Transfer Measurements. After filtering the temperature data with a Gaussian filter, accounting for curvature with fiducial marks, and performing a power balance as described in Sec. 3.2, the Nusselt number was computed at each pixel on all five sections. Figure 9(*a*) illustrates the Nusselt number at every point in the leading-edge-half of zone 1 (i.e., zone 1b) and shows decreased effectiveness radially away from the center of each impinging jet. Extraction areas can be seen in the dark blue regions between the double rows of impingement zones. These regions are characterized by lower convective HT coefficients on the interior surface of the shims because the flow of coolant is drawn away from the shim as it recirculates to another impingement zone. Figure 9(*b*) shows the variation in Nusselt number in the streamwise direction for zone 1b at *y* = 90, which includes several of the impingement holes. Figure 9(*b*) highlights the module-

to-module similarity and the significant variation at extraction regions. The coolant that is extracted from zone 1 is channeled to zone 2, as shown in Fig. 1. The HT results for zone 2 are provided inFigs. 9(*c*) and 9(*d*). The increase in Nusselt number at the centerline of the impingement holes in zone 2 as compared to zone 1 can be attributed to an increase in impingement hole velocity. The increased velocity is a result of mass conservation through fewer holes in zone 2 compared to zone 1.

Figures 9(*e*) and 9(*f*) illustrate the results for zone 3b, which is on the suction side of the vane and has no local extraction. All extraction is out the bottom of the test section as shown in Fig. 5(*a*). The Nusselt number at the centerline of the impingement jets in zone 3 is higher than impingement jets presented in Fig. 9(*a*). This increase in convective HT coefficient is primarily a result of zone 3b having fewer holes than zone 1b resulting in high centerline jet velocities for zone 3 due to conservation of mass of the coolant. It is also worth noting that the coolant within zone 3 is extracted in the streamwise direction, rather than being extracted between the rows of impingement holes. The extraction at the bottom of zone 3 results in the presence of crossflow. This crossflow can be observed in the top of Fig. 7(*a*) showing the velocity magnitude increasing as the coolant moves from left to right in the upper channel. While the impact of crossflow is minor compared to the effect of impingement cooling, the crossflow does enhance the HT between the rows of impingement jets, thereby increasing the spatially averaged Nusselt number. This improvement
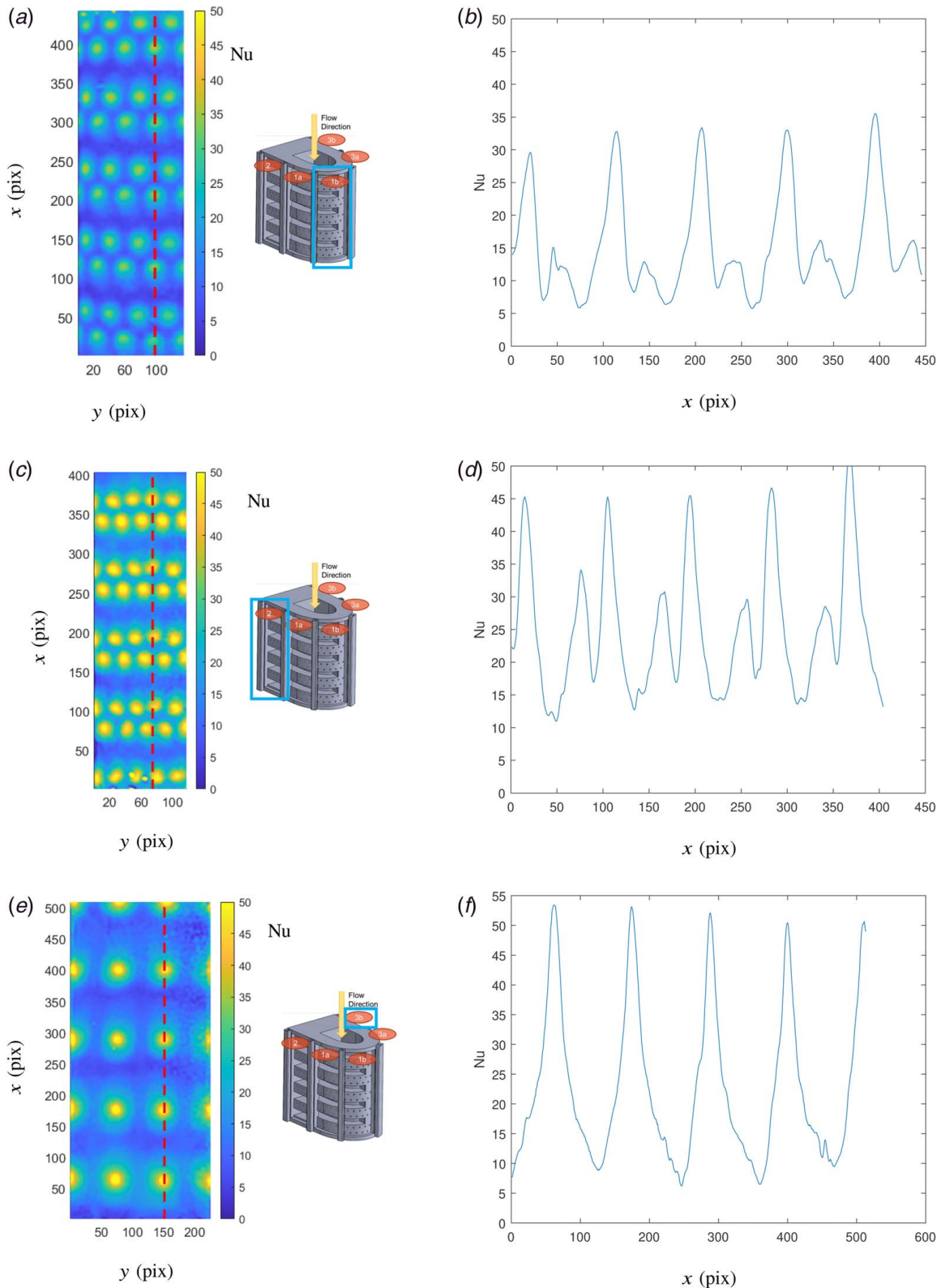
Fig. 9 Nusselt number distribution, zone 1b (top), zone 2 (middle), and zone 3b (bottom). Dashed vertical lines show the location for the Nusselt variation in the streamwise crossflow direction (root to tip) depicted at right. (*a*) Nusselt number, zone 1b. (*b*) Nusselt number variation, zone 1b. (*c*) Nusselt number, zone 2. (*d*) Nusselt number variation, zone 2. (*e*) Nusselt number, zone 3b. (*f*) Nusselt number variation, zone 3b.

between the impingement jets can be observed in Fig. 9(*e*) and is qualitatively demonstrated in the more gradual increase in each peak in Fig. 9(*f*), recalling the flow direction is right to left as displayed, as compared to Fig. 9(*b*).

Figure 10 is a HT comparison for each module within the various sections using a spatially averaged Nusselt number. There are several key takeaways from this figure. First, module-to-module variation shows a generally monotonic decrease following the
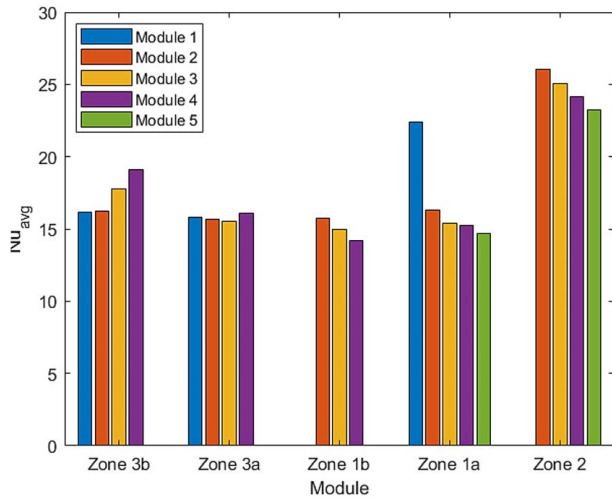
Fig. 10 Average Nusselt number across all modules and sections

Fig. 12 Streamwise variations of the ratio of crossflow to jet mass-flux (top) and predicted normalized Nusselt number variation (bottom) obtained from Eq. (4), where x is the radial direction within the vane (e.g., from root to tip). The crossflow mass-flux is determined via a mass balance applied to MRV measurements of jet velocities according to the analysis of Florschuetz et al. [16].

flow path for zones 1 and 2. The first module in zone 1a has the highest Nusselt number within zone 1, likely attributable to inflow effects. The view in Fig. 7(a) suggests that the core flow adjacent to zone 1a is quite fast which may increase the jet flowrates within this first module. Zone 3 results show the opposite effect from zones 1 and 2, with a monotonic increase in the average Nusselt number in the streamwise direction. This trend is most likely due to flow path differences: in zones 1 and 2, there are extraction channels between modules; in zone 3, the flow exits in the streamwise direction and enhances HT, an observation especially evident in zone 3b.

4.3 Magnetic Resonance Velocimetry and Heat Transfer Test Comparison.

By comparing the MRV and HT results, it is clear that the two experimental methods inform each other. As one example, Fig. 11 shows that peak Nusselt numbers are coincident with peak fluid velocities, consistent with forced convection theory. Likewise, the extraction regions in between each module of holes reveal low velocity flow, yielding a decreased HT rate and corresponding Nusselt number. Two lines are overlaid in Fig. 11 which correspond to the transverse plane in Fig. 7(b). The
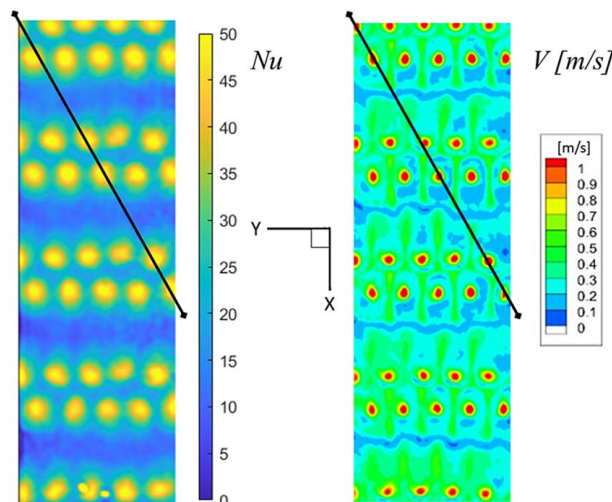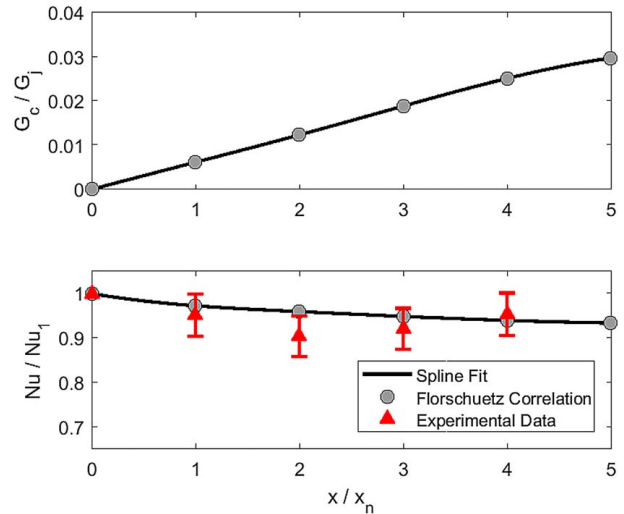

Fig. 11 Comparison of Nusselt number (left) and velocity profile (right) in zone 2, highlighting stagnating flow in extraction regions and corresponding decrease in HT rate

velocity plane is within the fluid and slightly off the vane wall surface; however, the HT measurements were made at the vane wall surface. The velocity field shows some periodicity across the plane with alternately faster and slower moving fluid that is not entirely uniform based on row location within the module. While subtle, this observation suggests that the flow within the zone is complex and three-dimensional. More important, this fine flow detail could be valuable in validating computational models. Further analysis of impingement surfaces in both datasets can inform future designs of the vane cooling insert system.

4.4 Comparison to Correlation.

Measurement of the complete three-dimensional velocity field within the vane cooling insert [28] and the surface HT distribution over each of the impingement zones provides a unique opportunity to evaluate the usefulness of existing durability design correlations for such flow situations. For example, the correlation of Florschuetz et al. [16] is widely used in the gas turbine industry to provide estimates of internal HT coefficients for impingement arrays with crossflow that have one downstream flow outlet. In the vane cooling impingement insert, this situation is obtained in zone 3. The impingement array in zone 3 is "inline" in the parlance of Ref. [16], so the ratio of local Nusselt number between the impingement holes (Nu) to that directly underneath the first row of the impingement array (Nu$_1$) is given by the correlation

$$\frac{\text{Nu}}{\text{Nu}_1} = 1 - 0.596 \left(\frac{x_n}{d}\right)^{-0.103} \left(\frac{y_n}{d}\right)^{-0.380} \left(\frac{z_n}{d}\right)^{0.803} \left(\frac{G_c}{G_j}\right)^{0.561} \quad (4)$$

where G_c/G_j is the ratio of the mass-flux due to crossflow between the rows in the streamwise direction to the mass-flux of the impingement jets. For comparison purposes, the coordinates are defined consistently with the work of Florschuetz: x_n is the streamwise jet hole spacing, y_n is the spanwise jet hole spacing, and z_n is the jet to hole spacing. In Ref. [16], the quantity G_c/G_j was evaluated based on conservation of mass arguments, and if that analysis is followed here taking into account the jet mass fluxes measured in the MRV experiments, it is possible to compare the correlation of Eq. (4) to the measurements obtained in the HT experiment. The results of this analysis are presented in Fig. 12 where the top plot is the variation of the quantity G_c/G_j versus streamwise distance normalized by the streamwise hole spacing. The bottom plot is an
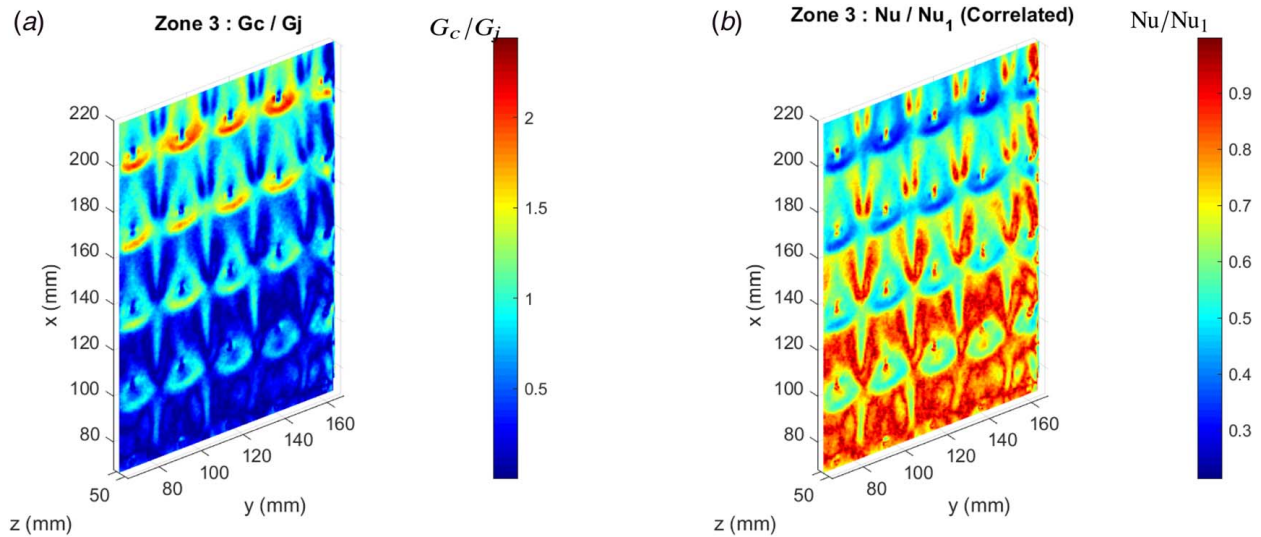
Fig. 13 Local variation of the ratio of crossflow to jet mass-flux evaluated from MRV measurements (left) and local variation of the quantity Nu/Nu1 determined via application of Eq. (4) to the G_c/G_j data given in left side subfigure (right). (a) zone 3, G_c/G_j and (b) zone 3, Nu/Nu_1.

evaluation of Eq. (4) for the values of G_c/G_j given in the upper plot. For comparison, data obtained in the HT experiment of this work are also plotted using results of Fig. 9(e). The experimental data were first averaged in the spanwise direction at all streamwise locations opposite to the impingement jets. The data were then normalized by the spanwise average obtained at the streamwise location of the first impingement row. These data were then plotted versus impingement row number in the bottom plot of Fig. 12, which illustrates correlated values of the Nusselt number compared to the measured variation of streamwise-averaged Nusselt numbers between impingement rows. One can see that the variation in mean Nusselt number from row to row is fairly well approximated by the correlated values. However, it should be noted that some of the impingement-array design parameters are on the limits of those used by Florschuetz et al. [16] to develop Eq. (4). In particular, the quantity $(y_n/d)(z_n/d) = 9.1 \times 3 = 27.3$ is larger than that used for any impingement array with $(z_n/d) = 3$ in Ref. [16]. Additionally, the quantity $(x_n/d)(y_n/d) = 13.2 \times 9.1 = 120.12$ is on the upper limit of impingement spacing measured by Florschuetz et al. [16]. Taken together, these impingement design parameters result in a small level of crossflow as seen in the upper plot of Fig. 12. Accordingly, the effect on the streamwise variation of the spanwise-averaged Nusselt number is also small.

While Eq. (4) does seem to allow for accurate design-level estimates of the spanwise-mean Nusselt number variation in the streamwise direction for impingement zone 3, it is not clear whether there is a rigorous way to apply the correlation of Florschuetz et al. [16] in a spatially resolved durability analysis. For example, Fig. 13(a) is a plot of the local mass-flux due to crossflow normalized by the impingement jet mass-flux over a portion of zone 3. One can see that the local mass-flux ratio can be locally very high, and if this local variation is evaluated according to Eq. (4) and plotted in Fig. 13(b), then there is a large local effect on the Nusselt number. This effect is not seen in the HT experiments of this work, and the spatial variation in Nusselt number obtained through this application of Eq. (4) is quite different from that measured experimentally. So, for the purposes of a turbine durability analysis that relies on the spatial variation of Nusselt numbers for a thermal boundary condition, perhaps it is better to apply the full map of HT coefficients measured in this HT experiment directly rather than relying on Florschuetz et al. [16] correlation. This is in part the method advocated by Downs et al. [50], which emphasized the need for rapid, complementary computational and experimental evaluation of advanced turbine durability designs.

4.5 Experimental Uncertainty. The MRI velocity measurements reported herein contain several sources of random, bias, and statistical error. Following the approach described in Ref. [17], the measurement uncertainty estimates for MRV used the standard deviation of the velocity in a region of interest (ROI) within the central feed channel of the experimental model. Uncertainty estimates employed a 95% confidence interval from a Student's t-test, calculated with a voxel-by-voxel approach and averaged over the ROI. The bias errors were calculated using the measured bulk velocity compared to a calibrated flowmeter. The two error sources were combined using a root sum of squares technique, with an overall uncertainty for the reported velocity measurements estimated to be 0.035 m/s, or $\pm 7\%$ of the peak velocity at the inlet to the feed cavity.

HT test uncertainty estimates were based on full field propagation of imposed errors in all key parameters. The authors estimate uncertainty to range from approximately 3% in the impingement zones to approximately 10% in the low HT zones. This estimate includes bias errors applied in dx, dy, external temperature (T_{ext}), voltage, thickness, thermal conductivity, emissivity, and natural convection as well as large (~ 1 K) single-pixel noise on temperature. Of note, the uncertainty shown for Fig. 12 was assumed to be $\pm 5\%$; future work will evaluate the spatial dependence of error to further refine the uncertainty estimate of Nu/Nu_1.

5 Conclusions and Future Work

Two novel, paired experiments were designed, conducted, and analyzed using MRV and steady-state IR imaging techniques. These methods provided high-fidelity velocity and HT data sets that can be used to validate computational simulations of the vane cooling forward insert and directly inform the design of the device's complex geometry and impingement cooling method. Velocity testing was conducted at a Reynolds number of 10,000. Velocity data showed some jet-to-jet variability and minimal module-to-module variation, a result with two notable outcomes. First, it confirmed the design decision to introduce a tip bleed in the MRV test section to more closely model the first modules featured in the vane cooling forward insert. Second, it revealed a degree of feed mechanism effectiveness, thereby eliminating the need to design a complex manifold shape in this dimension, a valuable observation for designers. HT datasets showed similar results along the impingement surfaces of the vane cooling insert.

Furthermore, the HT testing methods used in this study proved to be cost-effective compared to other techniques. Quantitative and qualitative comparisons of the paired tests' results showed strong agreement between flow velocity and cooling performance. Module-to-module variation in Nusselt number was evident, attributable to the complex interaction between transverse and impinging flows within the apparatus. Comparison with internal HT correlations using the data from Florschuetz et al. [16] showed reasonable agreement for some impingement-array design parameters. Measurement uncertainty was assessed and estimated to be approximately $\pm 7\%$ for velocity and ranging from $\pm 3\%$ to $\pm 10\%$ for Nusselt number.

Acknowledgment

Conflict of Interest

There are no conflicts of interest.

Data Availability Statement

The authors attest that all data for this study are included in the paper.

Nomenclature

d = jet hole diameter
k = thermal conductivity of impingement plate
x = streamwise direction of internal crossflow
I = electric current
T = temperature
V = voltage
$\dot{Q}$ = HT rate
x_n = streamwise jet hole spacing
y_n = spanwise jet hole spacing
z_n = jet plate to impingement hole spacing
G_c = crossflow mass-flux in the streamwise direction
G_j = impingement jet mass-flux
Gr = Grashof number
Nu = Nusselt number
Re = Reynolds number

Subscripts

cond = HT due to conduction
conv = HT due to forced convection
ext = external temperature
Joule = thermal energy generation due to Joule heating
natural = HT due to free convection
rad = HT due to radiation

References

[1] Eliaz, N., Shemesh, G., and Latanision, R., 2002, "Hot Corrosion in Gas Turbine Components," Eng. Failure Anal., **9**(1), pp. 31–43.
[2] Carter, T. J., 2005, "Common Failures in Gas Turbine Blades," Eng. Failure Anal., **12**(2), pp. 237–247.
[3] Taslim, M., Spring, S., and Mehlman, B., 1992, "Experimental Investigation of Film Cooling Effectiveness for Slots of Various Exit Geometries," J. Thermophys. Heat Transfer, **6**(2), pp. 302–307.
[4] Pai, B. R., and Whitelaw, J. H., 1971, "The Prediction of Wall Temperature in the Presence of Film Cooling," Int. J. Heat Mass Transfer, **14**(3), pp. 409–426.
[5] Miller, N., Siw, S. C., Chyu, M. K., and Alvin, M. A., 2013, "Effects of Jet Diameter and Surface Roughness on Internal Cooling With Single Array of Jets," Turbo Expo: Power for Land, Sea, and Air, Vol. Volume 3A: Heat Transfer, San Antonio, TX, June 3.
[6] Martini, P., Schulz, A., and Bauer, H. J., 2005, "Film Cooling Effectiveness and Heat Transfer on the Trailing Edge Cutback of Gas Turbine Airfoils With Various Internal Cooling Designs," ASME J. Turbomach., **128**(1), pp. 196–205.
[7] Lau, S. C., Cervantes, J., Han, J. C., and Rudolph, R. J., 2008, "Internal Cooling Near Trailing Edge of a Gas Turbine Airfoil With Cooling Airflow Through Blockages With Holes," ASME J. Turbomach., **130**(3), p. 031004.
[8] Goldstein, R. J., Eckert, E. R. G., and Burggraf, F., 1974, "Effects of Hole Geometry and Density on Three-Dimensional Film Cooling," Int. J. Heat Mass Transfer, **17**(5), pp. 595–607.
[9] Goldstein, R. J., 1971, "Film Cooling," Adv. Heat Transfer, **7**(1), pp. 321–379.
[10] Glynn, C., O'Donovan, T., Murray, D., and Feidt, M., 2005, "Jet Impingement Cooling," Proceedings of the 9th UK National Heat Transfer Conference, Manchester, pp. 5–6.
[11] Dannhauer, A., 2009, "ASME Turbo Expo 2009," Power for Land, Sea, and Air, Orlando, FL, June 8–12.
[12] Cunha, F., and Chyu, M. K., 2006, "Trailing-Edge Cooling for Gas Turbines," J. Propul. Power, **22**(2), pp. 286–300.
[13] Burns, W., and Stollery, J., 1969, "The Influence of Foreign Gas Injection and Slot Geometry on Film Cooling Effectiveness," Int. J. Heat Mass Transfer, **12**(8), pp. 935–951.
[14] Bunker, R. S., 2005, "A Review of Shaped Hole Turbine Film-Cooling Technology," ASME J. Heat Transfer-Trans. ASME, **127**(4), pp. 441–453.
[15] Jambunathan, K., Lai, E., Moss, M., and Button, B., 1992, "A Review of Heat Transfer Data for Single Circular Jet Impingement," Int. J. Heat Fluid Flow, **13**(2), pp. 106–115.
[16] Florschuetz, L., Truman, C., and Metzger, D., 1981, "Streamwise Flow and Heat Transfer Distributions for Jet Array Impingement With Crossflow," ASME 1981 International Gas Turbine Conference and Products Show, Houston, TX, Mar. 9–12, American Society of Mechanical Engineers, p. V003T09A005.
[17] Benson, M. J., Helmer, D., Van Poppel, B. P., Duhaime, B., Bindon, D., Cooper, M., Woodings, R., and Elkins, C. J., 2019, "Detailed Three-Dimensional Velocity Field Measurements of a Complex Internal Cooling Flow Within a Gas Turbine Vane," ASME International Mechanical Engineering Congress and Exposition, Vol. 7: Fluids Engineering, Salt Lake City, UT, Nov. 16–19.
[18] Singh, P., and Ekkad, S. V., 2017, "Effects of Spent Air Removal Scheme on Internal-Side Heat Transfer in an Impingement-Effusion System at Low Jet-to-Target Plate Spacing," Int. J. Heat Mass Transfer, **108**(A), pp. 998–1010.
[19] Onstad, A. J., Elkins, C. J., Moffat, R. J., and Eaton, J. K., 2009, "Full-Field Flow Measurements and Heat Transfer of a Compact Jet Impingement Array With Local Extraction of Spent Fluid," ASME J. Heat Transfer-Trans. ASME, **131**(8), p. 082201.
[20] Bunker, R. S., Dees, J. E., and Palafox, P., 2014, Impingement Cooling in Gas Turbines: Design, Applications, and Limitations, 1st ed., Vol. 25, WIT Press, Southampton, UK, pp. 1.
[21] Han, J.-C., 2004, "Recent Studies in Turbine Blade Cooling," Int. J. Rotat. Mach., **10**(6), pp. 443–457.
[22] Han, B., and Goldstein, R. J., 2001, "Jet-Impingement Heat Transfer in Gas Turbine Systems," Ann. N.Y. Acad. Sci., **934**(1), pp. 147–161.
[23] Clark, J., Koch, P., Ooten, M., Johnson, J., Dagg, J., McQuilling, M., Huber, F., and Johnson, P., 2009, "Design of Turbine Components to Answer Research Questions in Unsteady Aerodynamics and Heat Transfer, " Air Force Research Laboratory, Wright-Patterson Air Force Base, OH, Report No. AFRL-RZ-WP-TR-2009-2180.
[24] Ni, R.-H., Humber, W., Fan, G., Clark, J. P., Anthony, R. J., and Johnson, J. J., 2013, "Comparison of Predictions From Conjugate Heat Transfer Analysis of a Film-Cooled Turbine Vane to Experimental Data," ASME Turbo Expo 2013: Turbine Technical Conference and Exposition, San Anotnio, TX, June 3–7.
[25] Clark, J. P., Anthony, R. J., Ooten, M. K., Finnegan, J. M., Dean Johnson, P., and Ni, R. -H., 2018, "Effects of Downstream Vane Bowing and Asymmetry on Unsteadiness in a Transonic Turbine," ASME J. Turbomach., **140**(10), p. 101006.
[26] Johnson, J., King, P., Clark, J., and Ooten, M., 2014, "Genetic Algorithm Optimization of a High-Pressure Turbine Vane Pressure Side Film Cooling Array," ASME J. Turbomach., **136**(1), p. 011011.
[27] Johnson, J., Clark, J., Anthony, R., Ooten, M., Ni, R., and Humber, W., 2019, "3D Heat Transfer Assessment of Full-Scale Inlet Vanes With Surface-Optimized Film Cooling: Part 2—Conjugate CFD Simulations," ASME Turbo Expo 2019: Turbomachinery Technical Conference and Exposition, Volume 5B: Heat Transfer, Phoenix, AZ, June 17–21, American Society of Mechanical Engineers Digital Collection.
[28] Downs, J., 2012, "Air Cooled Turbine Airfoil With Sequential Cooling," US Patent 8,096,766.

[29] Pula, J., 2016, "Heat Transfer in the H.I.T Research Turbine," Turbine Energy Technology Symposium, Dayton, OH.

[30] Thurow, B. S., and Lynch, K. P., 2009, "Development of a High-Speed Three-Dimensional Flow Visualization Technique," AIAA J., **47**(12), pp. 2857–2865.

[31] Cornaro, C., Fleischer, A., and Goldstein, R. J., 1999, "Flow Visualization of a Round Jet Impinging on Cylindrical Surfaces," Exp. Therm. Fluid Sci., **20**(2), pp. 66–78.

[32] Elkins, C. J., and Alley, M. T., 2007, "Magnetic Resonance Velocimetry: Applications of Magnetic Resonance Imaging in the Measurement of Fluid Motion," Exp. Fluids, **43**(6), pp. 823–858.

[33] Stark, D., Bradley, W., and Bradley, W., 1999, *Magnetic Resonance Imaging*, Vols. 1 and 2, Mosby, St. Louis, MO.

[34] Brown, R. W., Cheng, Y.-C. N., Haacke, E. M., Thompson, M. R., and Venkatesan, R., 2014, *Magnetic Resonance Imaging: Physical Principles and Sequence Design*, John Wiley & Sons, New York.

[35] Elkins, C. J., Markl, M., Pelc, N., and Eaton, J. K., 2003, "4D Magnetic Resonance Velocimetry for Mean Velocity Measurements in Complex Turbulent Flows," Exp. Fluids, **34**(4), pp. 494–503.

[36] Ekkad, S. V., and Han, J.-C., 2000, "A Transient Liquid Crystal Thermography Technique for Gas Turbine Heat Transfer Measurements," Meas. Sci. Technol., **11**(7), p. 957.

[37] Satta, F., and Tanda, G., 2014, "Measurement of Local Heat Transfer Coefficient on the Endwall of a Turbine Blade Cascade by Liquid Crystal Thermography," Exp. Therm. Fluid Sci., **58**(1), pp. 209–215.

[38] Helmer, D. B., and Hoefler, F., 2015, "Steady IR Methodology for Leading Edge Impingement Measurements," ASME Turbo Expo 2015: Turbine Technical Conference and Exposition, Volume 5A: Heat Transfer, Montreal, Quebec, Canada, June 15–19, American Society of Mechanical Engineers Digital Collection.

[39] Anderson, J. B., McClintic, J. W., Bogard, D. G., Dyson, T. E., and Webster, Z., 2017, "Freestream Flow Effects on Film Effectiveness and Heat Transfer Coefficient Augmentation for Compound Angle Shaped Holes," ASME Turbo Expo 2017: Turbomachinery Technical Conference and Exposition, Volume 5C: Heat Transfer, Charlotte, NC, June 26–30, American Society of Mechanical Engineers Digital Collection.

[40] Dees, J. E., Bogard, D. G., and Bunker, R. S., 2010, "Heat Transfer Augmentation Downstream of Rows of Various Dimple Geometries on the Suction Side of a Gas Turbine Airfoil," ASME J. Turbomach., **132**(3), p. 031010.

[41] Chupp, R. E., Helms, H. E., McFadden, P. W., and Brown, T. R., 1969, "Evaluation of Internal Heat-Transfer Coefficients for Impingement-Cooled Turbine Airfoils," J. Aircr., **6**(3), pp. 203–208.

[42] Imbriale, M., Ianiro, A., Meola, C., and Cardone, G., 2014, "Convective Heat Transfer by a Row of Jets Impinging on a Concave Surface," Int. J. Therm. Sci., **75**(1), pp. 153–163.

[43] Goldstein, R. J., and Timmers, J., 1982, "Visualization of Heat Transfer From Arrays of Impinging Jets," Int. J. Heat Mass Transfer, **25**(12), pp. 1857–1868.

[44] Spalding, D. B., 1960, "A Standard Formulation of the Steady Convective Mass Transfer Problem," Int. J. Heat Mass Transfer, **1**(2), pp. 192–207.

[45] Saha, A. K., and Acharya, S., 2008, "Computations of Turbulent Flow and Heat Transfer Through a Three-Dimensional Nonaxisymmetric Blade Passage," ASME J. Turbomach., **130**(3), p. 031008.

[46] Laskowski, G., and Felten, F., 2010, "Steady and Unsteady CFD Simulations of Transonic Turbine Vane Wakes With Trailing Edge Cooling," Proceedings of the European Conference on Computational Fluid Dynamics, Lisbon, Portugal, June 14–17.

[47] Na, S., and Shih, T. I., 2007, "Increasing Adiabatic Film-Cooling Effectiveness by Using an Upstream Ramp," ASME J. Heat Transfer-Trans. ASME, **129**(4), pp. 464–471.

[48] Benson, M. J., Elkins, C. J., Mobley, P. D., Alley, M. T., and Eaton, J. K., 2009, "Three-Dimensional Concentration Field Measurements in a Mixing Layer Using Magnetic Resonance Imaging," Exp. Fluids, **49**(1), pp. 43–55.

[49] Bergman, T. L., Incropera, F. P., Lavine, A. S., and Dewitt, D. P., 2011, *Introduction to Heat Transfer*, John Wiley & Sons, New York.

[50] Downs, J., Fraga, Z., and Ni, R., 2019, "Advanced Component Cooling Design and Evaluation for Gas Turbines, " Air Force Research Laboratory, Wright-Patterson Air Force Base, OH, Report. No. AFRL-RQ-WP-TR-2019-0030.